NATIONAL AIR INTELLIGENCE CENTER

THERMAL BLOOMING DURING WIND TURBULENCE,
NUMERICAL MODEL OF ADAPTIVE-OPTICS SYSTEMS,
AND TRICHROIC BEAM SPLITTER FOR DEUTERIUM
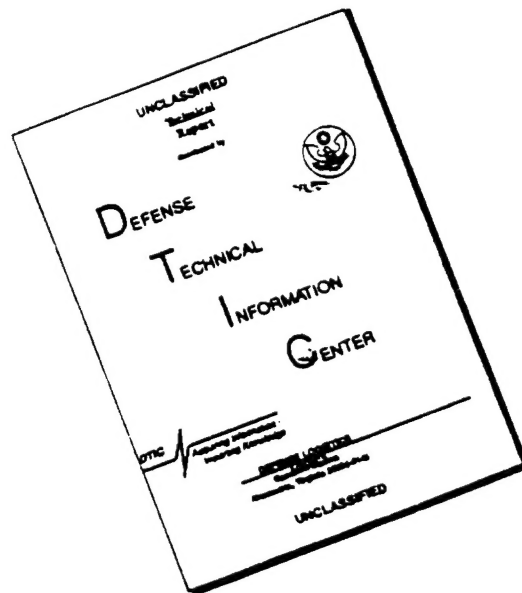FLUORIDE CHEMICAL LASERS

(Selected Articles)

19960408 189

DISCLAIMER NOTICE

THIS DOCUMENT IS BEST QUALITY AVAILABLE. THE COPY FURNISHED TO DTIC CONTAINED A SIGNIFICANT NUMBER OF PAGES WHICH DO NOT REPRODUCE LEGIBLY.

HUMAN TRANSLATION

NAIC-ID(RS)T-0508-95   11 March 1996

MICROFICHE NR: 96C000216

THERMAL BLOOMING DURING WIND TURBULENCE,
NUMERICAL MODEL OF ADAPTIVE-OPTICS SYSTEMS,
AND TRICHROIC BEAM SPLITTER FOR DEUTERIUM
FLUORIDE CHEMICAL LASERS (Selected Articles)

English pages: 44

TABLE OF CONTENTS

GRAPHICS DISCLAIMER

All figures, graphics, tables, equations, etc. merged into this
translation were extracted from the best quality copy available.

NUMERICAL STUDY OF THERMAL BLOOMING WITH WIND AND TURBULENCE AND ITS PHASE COMPENSATION

Zhang Tianshu, Lei Guangyu, Xie Lijuan,
and Zheng Shaotang

Beijing Institute of Applied Physics
and Computational Mathematics
P.O. Box 8009, Beijing 100088

CT In this paper we calculated numerically whole beam thermal blooming with
lence and their ideal phase compensation for laser atmosphere propagation usin
approximation 4D code, obtained the thermal distortions of laser beam for va
id analyzed the interation of thermal blooming with turbulence. In addition we also
ie selection principle of time step and space step.

ORDS   thermal blooming, turbulence, phase compensation.

I. Introduction

There are various favorable and unfavorable effects on laser beam transmission due to atmospheric conditions, mainly in variable wind force and variable direction relative to height in the atmosphere, such as random up-and-down motion of wind and turbulence in the atmosphere. Usually, winds are favorable to restrain thermal blooming; however, atmospheric turbulence mainly leads to the effect of beam expansion, and reduced beam

coherence. The paper presents various wind models. Turbulence is simulated with multiphase shield, with the application of the Kolmogorov spectrum. In section II, fundamental equations are given. In section III, the selection principle of time and space step lengths are discussed. In section IV, the results of calculations are listed along with a brief analysis. In section V, several conclusions are provided in the stages of the study.

II. Fundamental Equations

2.1. Equation of the Laser Electrical Field

The monochromatic and linearly polarized scalar wave equation is obtained in the paraxial approximation

$$\frac{-}{z} + \nabla_{\perp}^2 E + k^2 \delta \varepsilon E = 0$$

In the equation, $\frac{2\pi}{\lambda}$ is the laser wave number. In the paper, it is assumed that the wave numbers for the main laser and the beacon light are the same: $\frac{\partial^2}{\partial x^2} + \frac{\partial^2}{\partial y^2}$. The laser propagation direction is z. $\delta = 1$ corresponds to the main laser and $\delta = -1$ corresponds to the beacon light. The change $\delta\varepsilon$ of the dielectric constant in the atmosphere is due to thermal blooming and turbulence; the change

$$\delta \varepsilon_{TB} + \delta \varepsilon_{TURB}$$

Due to thermal blooming, the variable dielectric constant $\delta\varepsilon_{TB}$ is proportional to the variable density ρ_1; that is,

$$.46 \rho_1 (x, y, z, t)$$

2

Due to turbulence, the variable dielectric constant $\delta\varepsilon_{TURB}$ is obtained by the following processing of the equivalent phase shield: when the gap between the turbulence phase shield is not large (it should not be too small), otherwise there will be a statistical correlation between the two phase shields, the diffraction effect can be neglected. Therefore, from Eq. (1), we obtain the field equation for the case of pure turbulence, leaving out of consideration the thermal blooming effect,

$$zik\,\frac{\partial E}{\partial z} + k^2\delta\varepsilon_{TURB}E = 0$$

Thus, we obtain

$$\Delta z_{p.s.}) = E(z)\,e^{\frac{ik}{2}\delta\varepsilon_{TURB}\Delta z_{p.s.}}$$

In the equation, $\Delta z_{p.s.}$ [p.s.=phase shield] is the distance between the phase shields. From [1], we obtain

$$\int_{z}^{z+\Delta z_{p.s.}} \delta\varepsilon_{TURB}\,dz$$

$$\sqrt{\frac{2\pi}{\Delta z_{p.s.}}}\,\Phi\,e^{i(K_x x + K_y y)}a(K_x, K_y)\,dK_x\,dK_y$$

Here, Φ is the Kolmogorov spectrum. There is

$$K_z) = 0.033\,c_n^2(K_0^2 + K_x^2 + K_y^2 + K_z^2)^{-\frac{11}{6}}$$

In the equation, the turbulence structure constant C^2_n can vary with z. $\left(\dfrac{\pi}{L_0}\right)$, L_0 is the external dimension of turbulence. $a(K_x, K_y)$ is the two-dimensional complex random function. The other real and virtual parts are subject to the Gaussian distribution with 1 as variance, that is,

3

$$\text{Re}\,(a) = \sqrt{-2\ln r_i}\ \cos 2\pi$$
$$\text{Im}\,(a) = \sqrt{-2\ln r_i}\ \sin 2\pi$$

In the equation, $r \in (0, 1)$ is the pseudorandom number. To ensure that a is a real number, it is required that Re(a) and Im(a) satisfy, respectively, the conditions of mirror symmetry and mirror-reflection symmetry.

Eq. (5) explains the effect on turbulence of the medium in $\Delta z_{p.s.}$; this is equivalent to the phase shield that the phase change is $\varepsilon \quad \Delta z_{p.s.}$.

In the case of pure thermal blooming, the field equation is similar to Eq. (4), with the only difference being that is replaced with ε_T . The solution is similar to Eq. (5). Therefore, only the phase is changed in the pure thermal blooming that neglects the diffraction effect. Only when considering the diffraction effect (here, the term $\nabla^2 E$ is included in the field equation), then the phase change induces the change of oscillation amplitude.

2.2. Linearized Fluid-Mechanical Equations

By linearizing the fluid-mechanical equations, the following equations of mass, momentum, and energy are obtained:

$$\dot{\rho}_1 + \rho_0 \nabla \cdot \boldsymbol{u}_1 = 0$$

$$\frac{d\boldsymbol{u}_1}{dt} + \nabla p_1 = 0$$

$$- c_i^2 \frac{d\rho_1}{dt} = (\gamma - 1)\alpha_a I_p$$

4

In the equations, ρ_1, v_1 and p_1 are, respectively, the varying quantities density, velocity, and pressure. ρ_0 is the atmospheric temperature without turbulence. c_s is the speed of sound. However, γ_v is the ratio between the specific heats at constant pressure and at constant volume. α_a is the absorption coefficient. The equation of light intensity is

$$EE^* \qquad \text{(c is the speed of light)} \qquad (11)$$

The total derivative is

$$\frac{\partial}{\partial t} + \qquad V_x \frac{\partial}{\partial x} + V_y \frac{\partial}{\partial y}$$

In the paper, only the transverse-direction wind is considered. The authors used the four wind models given below:

1. x-direction constant wind: $z) = V_0$, $V_y(z$

2. x-direction variable wind: it is assumed that there is a linear relationship in $V_x(z)$, such as

$V_x(z)=V_0+\omega z$ (ω is a constant, which may indicate the rotational angular velocity of the beam, or may indicate a constant of atmospheric wind field varying with height).

3. Cyclostrophic wind:

$$V_x(z) = V_0(z)\cos\ldots$$
$$V_y(z) = V_0(z)\sin\ldots$$

We assume that $V_0(z)$ is a constant when only the wind direction changes with height for $\theta(z)=\beta z_0$.

4. Random wind

$$z, t) = V_x(z) + \delta V_x(x, y$$
$$z, t) = \delta V_y(x, y, z, t)$$

5

In the equations, the up-and-down motion (of the random wind) δV_x and δV_y are calculated with simulation processing that is similar to the simulation processing of $\delta\varepsilon_{TURB}$.

For the field equation (1), the authors applied two methods for its solution. One, it is to conduct a two-dimensional Fourier transform in the transverse direction. In the longitudinal-direction (propagation direction), the phase shield method is used for the solution of two levels of accuracy [1]. In the second method, the separation of components is used to divide Eq. (1) into multiple-component equations [2]. With respect to transverse-direction components, one-dimensional Fourier transform is conducted. For the longitudinal-direction, the analytical solution in form is sought.

The isobaric approximation is conducted with the fluid-mechanical equations. Then the three conservation equations degenerate into an equation of density variation:

$$V_x \frac{\partial \rho_\perp}{\partial x} + V_y \frac{\partial \rho_\perp}{\partial y} = -\frac{\gamma - 1}{c_s^2} \alpha_a I_p$$

III. Selection of Calculation Region and Lattice

3.1. Selection of L and N

To calculate for the functions of pseudo-transverse direction wind, and to reduce the boundary effect, the transverse-direction period L should be as large as possible, especially during large variations in functions. Since, based on the periodic boundary conditions, the spectral space lattice

6

interval   can be obtained (we make $\ldots$ $\ldots K$). It
can be seen that only when larger values of L are taken, can a
small-spectral lattice be obtained. However, the maximum
calculated wave number K^c_{max} $\ldots$ [c = calculated] (N is the
number of division points). We can see that if the high-
frequency portion is important in studying the problem, K^c_{max}
should extend to the high-frequency band. Thus, when L is large,
N is also large. Selection of L and N should be matched. We
take L=6a (a is the beam radius), thus $K^c_{max} \approx N/D$ (D=2a). With
respect to the Kolmogorov spectrum, during the centimeter-level
perturbation wavelength, the value of the spectral function has
been reduced so that it can be neglected. Therefore, when D is
approximately equal to 1m, N should be greater than 100 in order
to let K^c_{max} cover the main spectral band. Of course, with
respect to the problem of increasing small perturbations, due to
the large gain in short-wave perturbations, this is the
Kolmogorov spectrum, initially. Then very quickly, the high-
frequency portion will increase, thus N should be again
increased. However, N should not be too large because an
overlarge N will cause large calculation errors in the FFT
method.

3.2. Selection of Longitudinal-Direction Step Length Δz

When using the multiphase shield method at accuracy level 2,
the stability requirement is

$$1 \quad : \quad \frac{2\rho_0}{5.8 \times 10^{-4} |\rho_1| k}$$

when λ=1μm and under the isobaric approximation, there is

Here, MW/cm^2 is the unit for I_p; CGS units are used for the other quantities.

With respect to the separation of components method, the longitudinal-direction step length can be larger. We pick Δt between several to tens of meters.

3.3. Selection of Time Step Length Δt

With respect to the nonlinear dynamics problems, it is best to take the absolute stability format. For the rapidly varying stage, Δt should be as small as possible. Generally, Δt should be between 0.1 and 0.01 of the processing time. We select Δt=1/20(t_w); t_w=a/V_0 is the wind transition time.

IV. Calculation Results and Brief Analysis

In the calculations, we used the CGS units. The simplified model of large atmosphere transmission that we obtained is as follows: the homogeneous atmosphere at sea level of 5km thickness is used to simulate the total atmosphere in the laser path, and we assume that it is in the intermediate turbulent state. The homogeneous wind velocity is 500cm/s; the laser wavelength is selected as 1μm; and the laser beam radius is taken as 50cm. In the paper, the beam anomaly compensation adopts the ideal phase conjugate method.

8

4.1. Beam Rotation (Equivalent Shift Shearing Wind)

Let ω (rad/s) be equal to 2.6×10^{-3}, 5.2×10^{-3}, and 7.8×10^{-3} in three states: thermal blooming, thermal blooming with turbulence, and thermal blooming with turbulence and phase compensation, in the model calculations. Table 1 shows the calculation results.

For few models in Table 1, we compare the isobaric-approximation results in this research and the non-isobaric-approximation results in [3]. As discovered in the results the difference is minor at three times the wind transition time. It is apparent that isobaric approximation is a better approximation.

From Table 1, when I_p is large (also, the value of the thermal anomaly number N_D is large), the difference between thermal blooming and thermal blooming with turbulence is increased. This is because turbulence will induce intensity fluctuations δI (scintillation). From [4], we know the intensity fluctuation scale ‌. here f_B is the focal length of thermal blooming. When I_p is large, f_B is small, thus, I is also small. However, ‹ › . We can see that when I_p is large, the intensity fluctuation δI is also large. From Eq. (1), we know that large δI values will also induce large phase fluctuation values $\delta \Phi$, then the beam expansion effect is intensified. In other words, the larger the value of I_p, the more intensive interaction between thermal blooming and turbulence. Here the numerical calculation results also prove this point.

9

Brightest —point Strehl ratio S at target plane for three conditions. $t_{---}=3t_{--}$. condition A
bloomin g only B: Thermal blooming with turbulence, and C: thermal blooming and turbu
with ideal cpmpensation (the laser beam intensity I, is in W/cm², the slewing rate ω in r

ω	S I, Conditions	50	100	200	400	80ʊ
2.6 × 10⁻³	A	0.97	0.945	0.89 (0.89)	0.82[0.85]	
	B		0.71		0.55	
	C	0.94	0.91	0.89	0.79	
5.2 × 10⁻³	A	0.98	0.96	0.92 (0.92)	0.838[0.85]	0.65
	B	0.76	0.73	0.68	0.60	0.51
	C	0.96	0.95	0.93	0.92	0.82
⸲.8 × 10⁻³	A	0.984	0.97 [0.95]	0.935 (0.93) [0.93]	0.87 (?) [0.92]	0.75
	B	0.76	0.74	0.70	0.60	0.54
	C	0.952	0.945	0.93	0.90	0.88

·· mber in [   ] is presented by [3] ;
⸲mber in (   ) is obtained at $6t_{\omega}$.

From Table 1, we can see that phase compensation degrades in
the light-intensity range listed in the table. This is because
this range lies in the PCT region. From [5], we know that the
maximum compensable light intensity is

$$\varkappa'$$

In the equation $\varkappa' = \dfrac{}{2\pi}$ ($L_{\parallel}$ is the
transmission system). With respect to our model, F=314,

3W/cm². Therefore, $_{\varkappa}$ ` ⸲⸲50W/cm². The case is degraded
with more compensation when exceeding 50W/cm².

We know from the data listed in the table, the beam rotation
angular velocity ω varies by threefold, but the variation of the
Strehl ratio of the bright spots is not obvious. This is so

10

because the propagation distance in our model is relatively
short, and the equivalent shift shearing wind is not intense.
Furthermore, we can see that the turbulence effect is also
unrelated to the beam rotation speed.

From column 3 of Table 1 we know that there is little
difference in the calculation results at $3t_w$ and $6t_w$. Thus we
know that thermal blooming image has become stabilized at $3t_w$.

4.2. Cyclostropic Wind (Only Wind Direction Variation is Considered Here)

In the calculation, we take β (rad/cm) equal to 0.175×10^{-5}
($50°$ rotation at a 5km height). I_p [W/cm^2]=400. Other conditions
have been stated above. With respect to pure thermal blooming,
Fig. 1 shows the calculation results. From the figure, when the
image rotates by a certain angle, the extent of thermal anomaly
does not change because the thermal anomaly variation number

ν . With the wind velocity at constant and only
varying the wind direction, from our wind model we know

. Here N_D is

unrelated to β. In other words, N_D does not rely on the
variation of velocity or direction.

4.3. Calculation During High Thermal Anomaly Number

11

With respect to CW pulses, under the homogeneous medium conditions, the dimensionless thermal anomaly number is

(here, the unit of I_p is W/cm^2; CGS units are used for the other quantities). Here, $\quad$ (α_s is the scattering coefficient). For our model, when $I_p=800W/cm^2$, $N_D \approx 2500$. Now the phase difference is greater for adjacent lattice points. There will be greater error in calculations using the FFT method. Moreover, there are perturbations of varying scales at this time, as the relative importance of the high-frequency band of the spectrum is increased. Therefore, the number of lateral-direction division points should be at least greater than 200. In our calculations, 128 division points are applied. So there will be relatively larger errors for this light intensity. (Refer to the last column of Table 1, and Fig. 2.)

V. Conclusions

Here, the listed conclusions are the research accomplishments in steps. They are as follows:

5.1. There are intensive interactions among large light intensity (or intensive thermal anomaly), turbulence and thermal blooming. This results of scintillation amplified by thermal blooming.

5.2. For short wavelengths (1μm), low wind velocity, greater beam radius (in the vicinity of 1m), and longer propagation

12

distance (longer than several km) can compensate for low threshold of light intensity (below 100W/cm^2). Exceeding this threshold value, the situation will be degraded with more phase compensation.
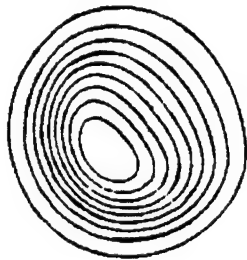

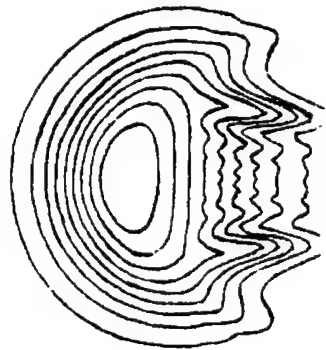An intensity contour at $3t_w$ ($I_p = 400$W/cm^2, rotation wind)

Fig. 2   An intensity contour at $3 t_w$ whe I_p (in W/cm^2) is 800

5.3. When the propagation distance is not long (less than several km), the variation in beam rotational angular velocity is several-fold. This renders little effect on the Strehl ratio of the bright points. Furthermore, the effect of turbulence is almost unrelated to the rotational speed.

5.4. With respect to a CW laser beam, the thermal blooming images have stabilized at threefold the wind transition time.

5.5. When wind velocity is constant, and wind direction changes only with height, the result rendered in the pure thermal blooming case is to rotate an angle for the entire thermal blooming image.

5.6. When there is high light intensity or intensive thermal anomaly, it is difficult to calculate thermal blooming by using the 4-D laser transmission program. Now there is physical

13

instability and also numerical instability; therefore, the horizontal and transverse-direction lattices should become slender and match to each other.

The authors are grateful to colleagues Lin Dewen and Xie Shumao for their beneficial comments on this research.

REFERENCES

Fleck JA et al. *Appl Phys*, 1976, **10**: 129.
Konyeav PA et al. *Appl Opt*, 1985, **24**: 415.
林德文等. 强激光大气传输中热晕及其补偿. 强激光与粒子束, 1993, 5(2): 253~2
Ulrich PB. Short course SC19, *SPIE* OE/ASE'91, (1991).
Smith DC et al. *SPIE*, 1991, **1408**: 112.

NUMERICAL MODEL FOR ADAPTIVE-OPTICS SYSTEM

Wang Yingjian, Wu Yi, and Gong Zhiben

Anhui Institute of Optics and Fine Mechanics,
Chinese Academy of Sciences, Hefei 230031

CT The model for simulating the components of an adaptive optics system is d‹ ιmerically applied to the laser beam propagation through turbulent atmosphere phase compensation. Results are given and disccused for compensated Streh with atmospheric coherent length anisoplanation and the finite bandwidth servo system. Also the variation of residual phase deviation *vs* d/r_0 is given :

‹JRDS adaptive optics, numerical simulation, turbulence, anisoplanation.

I. Introduction

As is well known, there are many successful experimental and applied examples of phase compensation of the turbulence effect on laser atmospheric transmission. As revealed in recent research, the interaction between turbulence and thermal blooming in the atmospheric transmission of high-powered lasers will lead to instability of phase compensation [1,2]. In fact, how many single components are required for an adaptive-optics system with a finite-bandwidth deformable mirror? With what kind of driver spacing, system response bandwidth, and other factors can one

15

attain the optimal phase compensation effect of laser atmospheric transmission? This series of problems remains to be answered. Thus, a numerical analytical model and a computational program are established for numerical simulation of the adaptive-optics system; this is important in studying the above-mentioned problems. Furthermore, this is an indispensable component part in the four-dimensional calculation mode of laser atmospheric transmission with compensation. On account of these factors, many scientists made outstanding investigations in this area [3,5]. The paper adopts the wavefront detection model similar to that proposed in [4,5]. As proposed in [3], in the wavefront reconstruction numerical model, the wavefront fitting method in the practical adaptive-optics system is similar to the method in reference [6]. On this basis, the computational program of numerical simulation was compiled, for simulation computation on atmospheric transmission of lasers with turbulence under phase compensation of the adaptive-optics system. Under identical compensation conditions, the Strehl ratio at the far-field of the light beam and the residue phase variance are entirely consistent with the simulation results in reference [3]. For the first time, the authors conducted computations on the phase compensation effect by finite response bandwidth of the adaptive-optics system with respect to different transmission aperture and anisoplanatism. The computational results are quite consistent with the analytical results. This explains that the analytical results of the simple theoretical results is reliable.
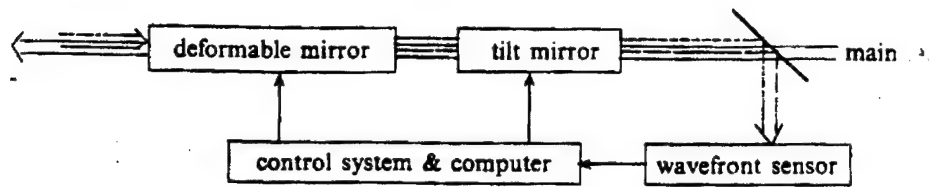
16

Fig. 1 A schematic diagram of adaptive optics system

II. Adaptive-Optics System and Its Numerical Model

Fig. 1 shows the principle of the adaptive optical portion in a laser transmission system. With respect to the anomalous wavefront phase of real-time measurement of the beacon light with the wavefront detector, the detection system calculates the corresponding driving quantity of the deformable mirror driver and the corresponding inclination of the tilt mirror, which is calculated based on the wavefront detector signal, to real-time drive of the deformable reflective mirror and tilt mirror, thus producing the phase wavefront conjugated with the beacon light phase to apply to the main laser in order to compensate for the wavefront anomaly of the main laser caused by atmospheric transmission during turbulence in order to improve light beam quality.

From Fig. 1, we can see that the adaptive-optics system includes mainly three major parts: (1) wavefront detector; (2) control system; and (3) tilt mirror and deformable reflective mirror (which is the wavefront reconstruction). In the following, the mathematical models and algorithms of these three

17

portions are introduced.

(1) Wavefront Detection

Generally, the dynamic Hartmann method is used for wavefront detection. The light spots gravities x_{cn} and y_{cn} of the beacon light on the focal plane of each Hartmann sublens are detected by the wavefront sensor. Thus, the corresponding wavefront tilt of the beacon light on the particular Hartmann sublens can be obtained.

$$= x_{cn}/F \quad , \quad \theta_{yn} = y_{cn}/F$$

In the equation, F is the focal length of the subaperture. In numerical simulation the light spot gravity is calculated with the following equation [4,5]

$$\int \text{Im}[\,\varphi_b^* \frac{\partial \varphi_b}{\partial x_n}\,]\,dr \Big/ \iint |\varphi_b|^2\, dr$$

$$\iint \text{Im}[\,\varphi_b^* \frac{\partial \varphi_b}{\partial y_n}\,]\,dr \Big/ \iint |\varphi_b|^2\, dr$$

n indicates the n-th sounding sublens; ϕ_b is the field function of the beacon light; k is the wave number of the beacon light. The integration region is the region of the sounding subaperture.

(2) Control System

Mainly, there are two functions for the control system. One is to use the wavefront tilt on the beacon mark thus detected to simulate the wavefront of the beacon light. Then the driving quantity of the driver for the deformable mirror is calculated. Secondly, this involves carrying out the hardware driving of the

18

deformable mirror. Here the first function is mainly discussed.
With respect to the second function, it is required to discuss
with the information control theory of the special system. In
numerical simulation, the simplest method is to introduce the
wavefront reconstruction error brought forth with the control
system in order to apply to the conjugate phase for processing.
In the first function, the wavefront trial fitting can adopt
multiple algorithms. For consistency with the simulation
algorithm [6] in the actual adaptive algorithm system, simulation
is carried out by using the Zernike polynomial. In this method,
first the wavefront of the beacon light is expanded into the
Zernike polynomial, and then the wavefront tilts on the various
sublenses are detected in order to obtain coefficients of various
terms of the expansion formula.

$$\vdots , y) = \sum_{i=3}^{M} a_i z_i(x, y)$$

M is the number of expansion terms in the Zernike polynomial.
Then the mean value of the wavefront inclination on the plane of
the n-th sounding sublens is

$$\int_{n} \sum_{i=3}^{M} a_i z_{ix}(x, y) dx dy / A$$

$$\int_{n} \sum_{i=3}^{M} a_i z_{iy}(x, y) dx dy / A$$

The integration region is the plane of the n-th sublens and its
area is A; the subscripts x and y of z_i indicate the partial
derivatives of x and y. In the Zernike expansion equation,

19

summation begins with the third term (i=3). This indicates that all the entire tilt items of the beacon light wavefront are separated because the main tilt reconstruction of the wavefront is accomplished by the tilt mirror. Similarly, the wavefront tilts θ_x and θ_y of the various sublenses thus detected are subtracted, respectively, from the total average tilts θ_x and θ_y of the wavefront. Thus we obtain

$$\overline{\theta}_x \quad , \quad \theta'_{yn} = \theta_{yn} - \overline{\theta}_y$$

$$\sum_{n=1}^{N} \theta_{xn} \quad , \quad \overline{\theta}_y = \frac{1}{N} \sum_{n=1}^{N} \theta_{yn}$$

Let

$$= \sum_{n=1}^{N} (\overline{\theta}_{xn} - \theta'_{xn})^2 + \sum_{n=1}^{N} (\overline{\theta}_{yn} - \theta'_{yn})^2$$

is the wavefront tilt variance. Solve for $\partial \sigma_\theta^2 / \partial a_j$ and let •z be equal to zero, and then we obtain

$$_{ln}]_{M \times N} [z_{ynm}]_{N \times M} \} [a_m]_M = [z_{xln}]_{M \times N} [\theta'_{xn}] + [z_{yln}]_{M \times N} [\theta'_{yn}]$$

In the equation

$$(x,y)dxdy/A \quad , \quad z_{yln} = \iint_n z_{yl}(x,y)dxdy/A$$

$[z_{xln}]$ and $[z_{yln}]$ are, respectively, the transposed matrixes of $[z_{xnm}]$ and $[z_{ynm}]$. By solving the linear equation (8), we obtain the developed coefficients of various orders of Zernike to be substituted into Eq. (3) to obtain the beacon light wavefront. This wavefront simulation algorithm is called the mode algorithm. We also conducted experiments on other wavefront simulation

20

algorithms (regional method). This is also feasible as indicated in the results of numerical calculations, as the wavefront simulation errors are basically compatible to the mode simulation algorithm of the Zernike polynomial. So these are omitted here. The calculation steps for the driving quality of the deformable mirror are as follows: first, the wavefront to be reconstructed is expanded into the linear superposition of the mirror surface function (which is also called the influence function) of the deformable mirror [3].

$$, y) = \sum_{i=1}^{N_A} d_i I_i(x, y) \qquad (10$$

N_A is the total number of drivers in the deformable mirror. d_i is the driving quantity of the i-th driver. $I_i(x,y)$ is the mirror surface function of the deformable mirror at its position. $I_i(x,y)$ can use the measured value of the surface type, or is described in the form of functions. When describing it is in the form of functions, generally all the surface type functions at the driver position are unified into a function form. In the actual system, of course, certain errors will exist. Here, we apply the gaussian function to describe the surface of the deformable mirror.

$$\frac{r^2}{p^2}]$$

; x_i and y_i are the position coordinates of the i-th driver; d is the mean spacing of two adjacent drivers; p is the coupling coefficient. In other words, when the driving quantity of this particular driver is one unit and when

21

the drivers at the adjacent positions do not act, thus it is the deformation quantity on the surface of the deformable mirror. In the following, the variance σ_{φ}^2 between the reconstructed wavefront and the beacon light wavefront (simulated wavefront) is used to solve for the reconstructed beacon light ϕ_s under the least-squares constraint:

$$\sigma_{\varphi}^2 = \iint [\varphi_s(x,y) - \varphi_b(x,y)]^2 dxdy$$

The integration region is the entire surface of the deformable mirror. Let $\dfrac{\partial \sigma_{\varphi}^2}{\partial} = 0$, we obtain [3]

$$\iint \varphi_s(x,y) I_j(x,y) dxdy = \iint \varphi_b(n,y) I_j(x,y) dxdy$$
$$(j=1,2,\cdots,N_i)$$

When written in the matrical form, this is

$$N_i = [I_{ij}]_{N_A \times N_A}^{-1} [R_j]_{N_A}$$

In the equation,

$$\iint \varphi_s(x,y) I_j(x,y) dxdy$$

$$\iint \rho_b(x,y) I_j(x,y) dxdy$$

$[I_{ij}]$ and $[R_j]$ are called, respectively, the influence function matrix and the simulation matrix.
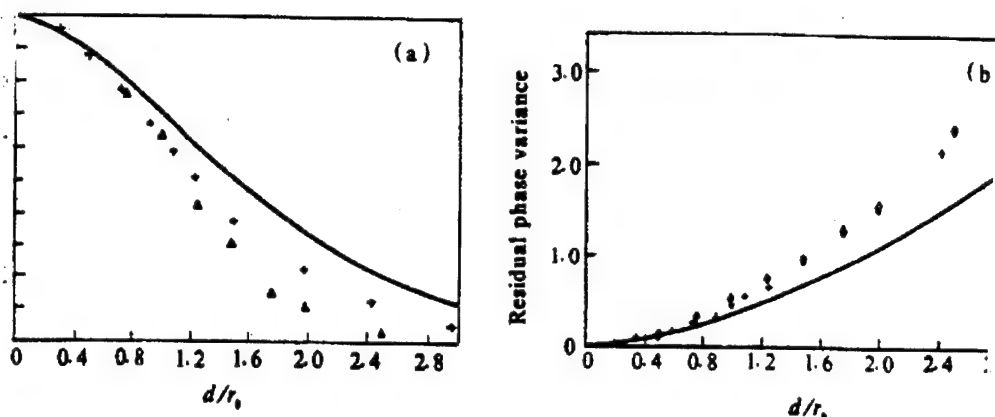

(3) Wavefront reconstruction

The wavefront reconstruction of the tilt mirror in the

22

numerical model is obtained by integrating the mean tilts of Eq. (10) from Eq. (6). The wavefront reconstruction of the deformable mirror is obtained by substituting into Eq. (10) the driving quantity obtained from Eq. (14). In the actual system, the wavefront reconstruction principle is accomplished by the control system driving hardware (tilt mirror and deformable reflective mirror). Here, naturally a certain control error exists. As revealed by analysis in reference [3], the term of the largest phase compensation error in the adaptable system is from the wavefront reconstruction of the deformable mirror. Generally, this is several times to tens of times greater than the control error. We can see that the effect is very little in the results of numerical simulation by neglecting the control error.

III. Results of Numerical Simulation

Based on the above discussion on model and calculation method, a numerical simulation program is compiled, to conduct simulation computations to compensate for the turbulence effect on laser atmospheric transmission in a 37-component adaptive-optics system. Under the turbulence effect, solving of the optical wave transmission equation adopts the phase shield method. The spectral inverting transmission of the turbulence phase shield applying the folded-type FFT algorithm as the wavelength of the beacon light is the same as the main laser wavelength $\lambda = 0.6328\mu m$).

23

For convenience in comparison, the same parameters in reference [3] are selected with coupling coefficient p=0.15. In the numerical calculation, the phase distribution of the beacon light can be obtained directly. Thus, from Eqs. (14) to (16), the driving quantity of the driver for the deformable mirror can be solved. In other words, this is to directly apply the beacon light phase to conduct wavefront reconstruction calculations; in other words, this is the detection and trial-fitting approach to obtain the error in the absence of a wavefront. The wavefront reconstruction residue variance and the Strehl ratio that are obtained are consistent with the results of numerical simulation in [3]. As shown in solid curves in Fig. 2a and b, the abscissa is d/r_0; r_0 is the transverse-direction coherent length of the atmosphere. The data point + and Δ(diamond-shape) indicate, respectively, the numerical simulation results when the emission apertures D are 1.67m and 0.25. Moreover, consideration is given to the wavefront detection and wavefront trial-fitting errors. In other words, the wavefront inclination is calculated with the beacon light field by using Eqs. (1) and (2). Then, from Eqs. (3), (8), and (9), the wavefront reconstruction calculation is conducted after wavefront trial fitting. From Fig. 2, we can see the following: (1) by leaving out of consideration on the wavefront detection and trial fitting error, this is obviously an overestimate of the effect of phase compensation, especially when d/r_0 is greater. When d/r_0=3.0, the wavefront detection error and wavefront trial-fitting error are only smaller by about one-

24

ulation $D=1.67$m ; $\triangle$ simulation $D=0.25$m $+$ simulation $D=1.67$m ; $\lozenge$ simulation $D=0.2$

considering error of wave−front reconstruction (b)wave−front reconstruction error (numerical

Fig.2 Strehl ratio (a) and residual phase variance vs d/r_0

half of the wavefront reconstruction error.   (2) Similarly, under

the condition of the same d/r_0, but different emission aperture,

although there is no obvious difference in the residue phase

variance (as shown in Fig. 2b), the phase compensation effect is

different, especially so in the case of more intensive turbulence

(larger d/r_0).   Possibly, the main reason is as follows: when D

is smaller, under the condition of intensive turbulence,

fluctuation of the oscillation amplitude will obviously reduce

the compensation efficiency of the AO system.   However, when D is

larger but d/r_0 remains unchanged, turbulence is weaker.   Thus,

together with the aperture-smoothing effect, fluctuation of

oscillation amplitude will be reduced.   Therefore, the effect of

AO compensation is better.

Fig. 3 shows the effect of anisoplanatism with regard to

phase compensation efficiency of the AO system.   In the figure, θ

twenty-two spaces is the isoplanatic angle [8]; θ is the included

angle between the beacon light and the main laser; the solid

25

curve indicates the results of the theoretical analysis [8]; and
the longitudinal coordinates indicate the relative Strehl ratio.
This is the result after normalizing the Strehl ratio when $\theta=0$.
Thus, it is convenient to compare with the theoretical result
[8]. Since no consideration was given in the theoretical
analysis to the effect of the number of limited components and
fluctuation of oscillation amplitude, this the entire phase
conjugate compensation. From the figure, the numerical
simulation result matches very closely with the theoretical
analytical result. When $\theta/\theta_0=1.0$, the relative Strehl ratio is
approximately 0.78. In other words, in these critical
isoplanatic conditions, the compensation efficiency of an actual
system is lower by 22% than the compensation efficiency of the
entire phase conjugation ($\theta=0$) at the instantaneous response. In
the condition of different d/r_0, the relationship between the
relative Strehl ratio and θ/θ_0 is basically consistent.

To conduct a simulation analysis on the effect of
compensation efficiency by time response bandwidth in an
adaptive-optics system, we should consider the turbulence phase
shield varying with time. We know that under the approximate
conditions established by Taylor's assumption, the variance of
turbulence with time can be converted into variation of
translation of wind speed with space. Therefore, we will apply
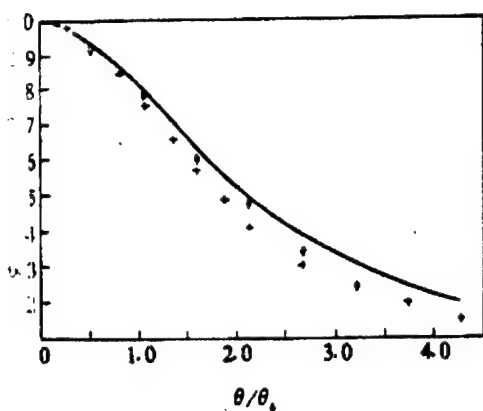the translation of wind speed with the turbulence phase shield to

26

Fig. 3 Relative Strehl ratio vs θ/θ_0

图 3 非等晕性对 Strehl 比的影响

—theory ; + simulation $d/r_0 = 1.0$
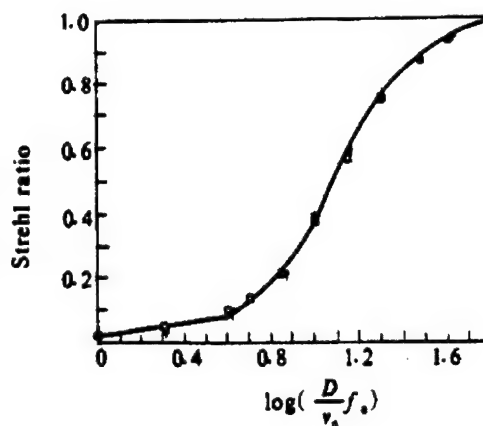
◇ simulation $d/r_0 = 2$

Fig. 4 Strehl ratio vs servo bandwidth at d

图 4 系统有限带宽对 Strehl 比的影响 (d/r_0

—Theory ; □ simulation $D = 1.0$m

+ simulation $D = 0.48$m

simulate variation with time [4]. Besides, it is still generally true that the response bandwidth of the adaptive-optics system can be simplified into a rectangular function. In other words, this corresponds to the time lag $\Delta t = 1/f_0$. f_0 is the response interruption frequency of the adaptive-optics system. Fig. 4 shows the comparison of the results between numerical simulation and theoretical analysis [8]. In the figure, the relative Strehl ratio shown is the Strehl ratio under the instantaneous response compensation conditions. The Strehl ratio is then normalized as a vector. The purpose is to eliminate the effect on the Strehl ratio due to residue phase difference in the actual system because of oscillation amplitude fluctuations and limited components. This effect has been described in Fig. 2. Thus, the effect on the Strehl ratio due to the system response bandwidth is revealed. In the figure, nu$_0$ indicates the mean wind speed; the value of d/r_0 is 1.0. The solid curve in the figure indicates the result of theoretical analysis (in the case of pure

27

conjugate phase compensation). We can see that the result of numerical simulation after normalization is quite consistent with the theoretical analytical results. In other words, it is rational to use the wind speed translation model to describe the time correlation of turbulence. Besides, if the space correlation scale l=2DELTAx is used for the turbulence, the scale is the reciprocal number of the Nyquist sampling frequency, and Δx is the transverse-direction calculated sampling width. Under Taylor's assumptions, the characteristic frequency (of turbulence) is $f_T=$ . . Then when $f_0=f_T$, the relative Strehl ratio is approximately 0.88, which is wholly consistent with the value from theoretical analysis [8]. In other words, by using the space relationship of turbulence to describe its characteristics, this provides a convenient and feasible means in studying the effect on compensation efficiency due to the response bandwidth of the adaptive-optics system.

IV. Conclusions

In this paper, the numerical model and algorithm of an actual adaptive-optics system are described. Under the same calculation conditions, the numerical calculation results fully match the results from numerical simulation in [3]. The effects on compensation efficiency by different emission apertures D, atmospheric coherent length r_0, and anisoplanatism, the system limited response bandwidth is very consistent with the results predicted from theoretical analysis. With regard to other

28

factors of influence in the adaptive-optics system, such as
coupling coefficient, mirror surface response function, and
variations in the inhomogeneous atmospheric conditions in the
actual case, the analysis of compensation efficiency in the
adaptive-optics system is a problem requiring further and deeper
research. However, the numerical calculation with compensation
experiments in the actual system will be an important means of
further improving the simulation model. Moreover, in the
theoretical models [6] in the paper and the other models
compared, it is simpler to describe the adaptive-optics transfer
function. Therefore, eventually the experimental results should
be relied on when examining the numerical model. This is the
next step in research.

The first draft of the paper was received on April 20, 1993;
the final revised draft was received for publication on July 16,
1993.

REFERENCES

arr TJ. *J. O. S. A*. 1989, AQ(7): 1038 ~ 1048.

知本，王英俭，吴毅. 光学学报. 1993, 13(5).

yson RK. *Optical Engineering*. 1990, 29(11): 1165

chonfeid JF. *SPIE*, 1990, 1221: 128 ~ 131.

lam RM. *SPIE*, 1990, 1221: 157 ~ 165.

文汉等. *SPIE, Proc*, 1990, 1271: 82 ~ 93.

E英俭，吴毅. 强激光与粒子束. 1992, 4(4): 581 ~

Tyler GA. *SPIE Proc*, 1983, 410: 179 ~ 188.

HIGH-PERFORMANCE TRICHROIC BEAM SPLITTER FOR DEUTERIUM FLUORIDE CHEMICAL LASERS

Xiong Shengming and Zhang Yundong
Institute of Optics and Electronics,
Chinese Academy of Sciences
P. O. Box 350
Shuangliu, Chengdu

:ACT The optical performance of trichromatic beam splitters developed for DF lase.
as shared—aperture components is presented . In this paper , we have discus
ite of splitter optical elements meeting spliting performance ,the selection of coating
multilayer film design and techniques ,and the performance results measured . The exp
ults of $R > 99.6\%$ at 3.8μm wavelength , the average transmittance of more than 0.7
avelength 8 ~ 14μm and the average transmittance of more than 0.50 at the CCD r;
for the trichromatic splitting film with uncoated back surface of ZnSe substrate
. The environmental stability of the samples are examined .
NORDS DF laser, share—aperture components, trichromatic coating, CVD ZnSe sub,.

I. Introduction

High-performance trichroic beam splitters are used in shared-aperture infrared DF (deuterium fluoride) chemical lasers. The beam splitter requires low-absorptance film-coating material. Such shared-aperture device has a total-reflection DF laser wavelength band. Moreover, the splitter has dual functions of easily transmitting CCD spectral response and a long-wave infrared spectrum between 8 and 14μm. The shared-aperture system

31

has the advantages of higher resolving power and signal-to-noise ratio. Moreover, the shared optical path in the system simplifies optical collimation and tracking. However, it is very difficult, experimentally, to share the multichroic film of the shared-aperture optical component. J. E. Rudisill et al. fabricated a dichroic beam splitter with reflection at 3.8μm and transmittance between 8 and 14μm [1]. To fabricate the trichroic beam splitter, it is required to deposit a multilayer film medium on a highly transparent substrate from the visible-light waveband to the infrared waveband (14μm). To upgrade the optical performance and the film layer system, the absorption inside the substrate and at the surface should be as small as possible.

The article discusses the design and preparation of the shared-aperture trichroic beam splitter. In experiments on the trichroic beam splitter film, there is reflectivity of greater than 99.6% at the 3.8μm DF output band. In the CCD optical region between 0.64 and 0.92μm, the mean transmittance is approximately 50%; between 8 and 14μm of infrared, the mean transmittance is greater than 75%.

II. Selection of Substrate and Film-Coating Materials

As a substrate material for the shared-aperture device in the DF laser system, it was required to have high transparency in the visible-light region and the long-wave infrared region, in addition to good mechanical strength. There are very few materials capable of transmitting in the visible light region and

also transmitting in the window (8 to 14µm) infrared region. The most commonly used materials are ZnSe, ZnS, BaF$_2$, alkali metal halides, and diamond. Although alkali metal halides have the optical properties of high transparency from the ultraviolet to the long-wave infrared region, still their mechanical strength and environmental stability are very poor. Diamond is expensive and large diamonds are even rarer. Transparency in the visible light region for large CVD ZnS is low; its mean transmittance is lower than 40% between 0.5 and 1.0µm. Moreover, in the visible light region, the transmittance curve varies with inclination [2]. From 0.6 to 17µm, CVD ZnSe is highly transparent. BaF$_2$ is transparent up to 12µm, then transparency begins to decrease. At 14µm, transparency is chancy.

For chemical vapor phase deposited large ZnSe pieces, Table 1 shows their mechanical properties. Fig. 1 presents a curve showing the CVD Raytran ZnSe optical spectrum as plotted experimentally at Raytheon Corporation in the United States. For large pieces of ZnSe material, its absorptance is very low; between 3.8 and 5.25µm, its absorption coefficient is 4x10^{-4}cm^{-1}.

For BaF$_2$ and ZnSe, both materials can be used as the window material of the shared-aperture window optical device. In the authors' research, ZnSe was used as the substrate. In the shared-aperture spectroscopic device, the substrate should be highly transparent in the visible light region and in the infrared region. In addition, its film-coating material should

33

Table 1 Typical properties of CVD ZnSe[1]

g/cm³)	5.27	index of refraction inhomogeneity
? (μm)	70	(ppm, max)
trength (psi,		temperature coefficient
t loading),	7500	(dn/dT ℃) at 10.6μm
modulus (psi)	9.75×10^4	extinction coefficient
ratio	0.28	@ 632.8nm (cm⁻¹)
(Knoop 50gm)	100	@ 1.06μm (cm⁻¹)
γ (Ω – cm)	~ 10^{12}	bulk absorption coefficient
expansion/ ℃		@ 2.77μm (cm⁻¹)
: 20 ~ 170℃	7.57×10^{-6}	@ 3.8μm (cm⁻¹)
conductivity (25℃, cgs)	0.043	@ 5.25μm (cm⁻¹)
eat (cal/gm ℃)	0.081	@ 10.6μm (cm⁻¹)
transmission 8~13μm	>70%	pulse damage threshold,
sion limits	0.5 ~ 22μm	peak intensity (GW cm²)
index		@ 180 ns
3 μm	2.417 ~ 2.385	@ 2.7μm
μm	2.403	@ 10.6μm

also be highly transparent in both regions. At the wavelength 3.85μm of the laser device, its absorptance is very low. Fig. 2 shows the absorptance at 3.8μm for some film layer. Thus, ThF_4, PbF_2, and YbF_3 can be selected as the film-coating materials. Since NaCl, KCl, and BaF_2 are easily softened by absorbing moisture and since YbF_3 film is very highly stressed, these materials are not readily mutually compatible. Finally, the highly refractive film-coating materials ZnSe and ZnS were chosen.
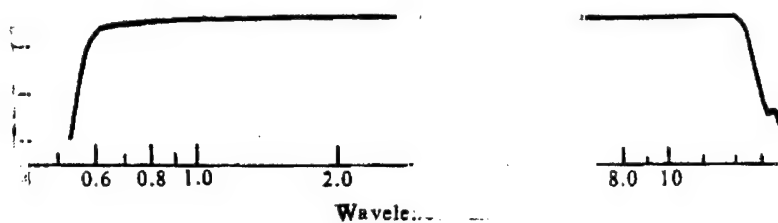
III. Design of Multilayer Film

Fig. 1 Typical transmittance of C   (20mm thick)

Any periodic multilayer film has a reflection band and a transmission band. The necessary condition for a reflection band is

In other words, the summation of the optical thicknesses of various film layers in the fundamental period are 1/2 of the integer times the center wavelength λ_O. In the equation, $n_i d_i$ is the optical thickness of the i-th layer in the fundamental period; q is the integer. λ_0 is the center wavelength possibly appearing in the reflection band. However, the above-mentioned conditions are insufficient. For certain wavelengths, although the summation of film thicknesses in the fundamental period is a multiple of 1/2, yet only when the thickness of various layers are an integer times 1/2 the wavelength λ_0, can the various film layers seem to disappear, as is also the case for the fundamental period and the entire film system with respect to the transmission band corresponding to these wavelengths. Therefore, based on Eq. (1), the center wavelength of the reflection band

35

can be determined, and the transmission band can also be determined. For the shared-aperture trichroic spectroscopic film, it is required that the reflection band be at the center wavelength λ_0=3.8μm. Moreover, it is required to have transmission in the spectral response region (6.0 to 6.90μm) for the CCD camera. In other words, this is required that the center range of the wavelength $\lambda_0/5$=0.76μm be in the transmission band. With respect to the standard quarter-film stack, this wavelength region is the reflection band, not up to the requirements of the spectroscopic properties. If the standard quarter-film stack is not used, the nonstandard film system can result in a transmission band between the 0.76μm center region and the infrared region between 8 and 14μm, while the 3.8μm wavelength region is the reflection band. For simplicity in preparation, and as few as possible film-coating materials to be used, two film-coating materials are used to design the film system in achieving the spectroscopic properties. Following this design, film systems of the four following periods can meet the requirements of spectroscopic properties: 4 32s. H represents a ZnSe film at one-quarter of refractance at 3.8μm wavelength; L is the PbF_2 or ThF_4 film at low one-quarter refractance.

The summation of the optical thicknesses of the various film layers in the fundamental period is

With the reflection band L appearing, the center wavelength satisfies the condition

36

With respect to g=5, 10, ..., that is, wavelengths of $\lambda_0/5$, $\lambda_0/10$, ..., each film layer seems to be nonexistent. Therefore, the multiple film layers in the fundamental period and composed of the fundamental period seem to be nonexistent. Therefore, these wavelengths corresponds to the transmission band. Obviously

g=1, 2, 3, 4, 6, 7, ..., reflection band

g=5, 10, ..., transmission band

In other words, in the region $\lambda_0=3.8\mu m$ wavelength is the reflection band; and the region $\lambda_0/5=0.76\mu m$ corresponds to the transmission band. For the absorption rate in the DF laser waveband to be lower than 0.05%, the film-coating material was selected so that it has low absorptance at the 3.8μm wavelength, thus reducing the thickness of the entire film system. For reflectance in the 3.8μm wavelength band to be at the maximum and transmittance to be reduced to less than 0.1%, with the minimum number of film layers, it is required that both film coating materials have a refractance ratio as high as possible. With consideration given to the laser damage threshold value, the outermost layer should be the low-absorption layer; its electric field intensity should be low. Therefore, two kinds of film structures $\frac{4}{c} \div l$ and , can be used as the fundamental period of the multilayer film for the shared-aperture device. By using $\lambda_0=0.76\mu m$ as the reference wavelength for the design,
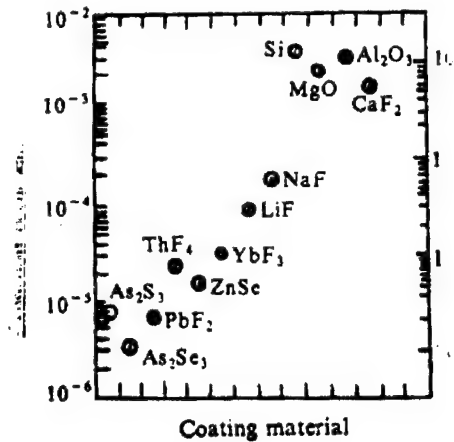
3. 2   3.8μm absorption in single-layer f
on CaF, substrates[4]

while the fundamental period becomes 4L6H and 6H4L, the 12-pair

multilayer film structure Sub/$(4L6H)^{12}$/Air (composed of PbF_2 and

ZnSe on a ZnSe substrate) should have its theoretical spectrum

response curves as shown in Fig. 3; the incidence angle of the

light beam is 22.5°.

Fig. 3a indicates the transmittance of the wavelength

response in the DF laser. Fig. 3b and 3c show the CCD spectral

responses and the 8 to 14μm transmittance curves. With respect

to the wavelength between 8 and 14μm, we do not expect that the

theoretical calculations are accurate because the optical

constants of the film coating materials in this spectral region

are uncertain.

In Fig. 3b and 3c, the spectral response does not include

the effect of reflectance at the back of the ZnSe substrate

(theoretically, over 17%) of the beam splitter.

At the back of the beam splitter, we should deposit a

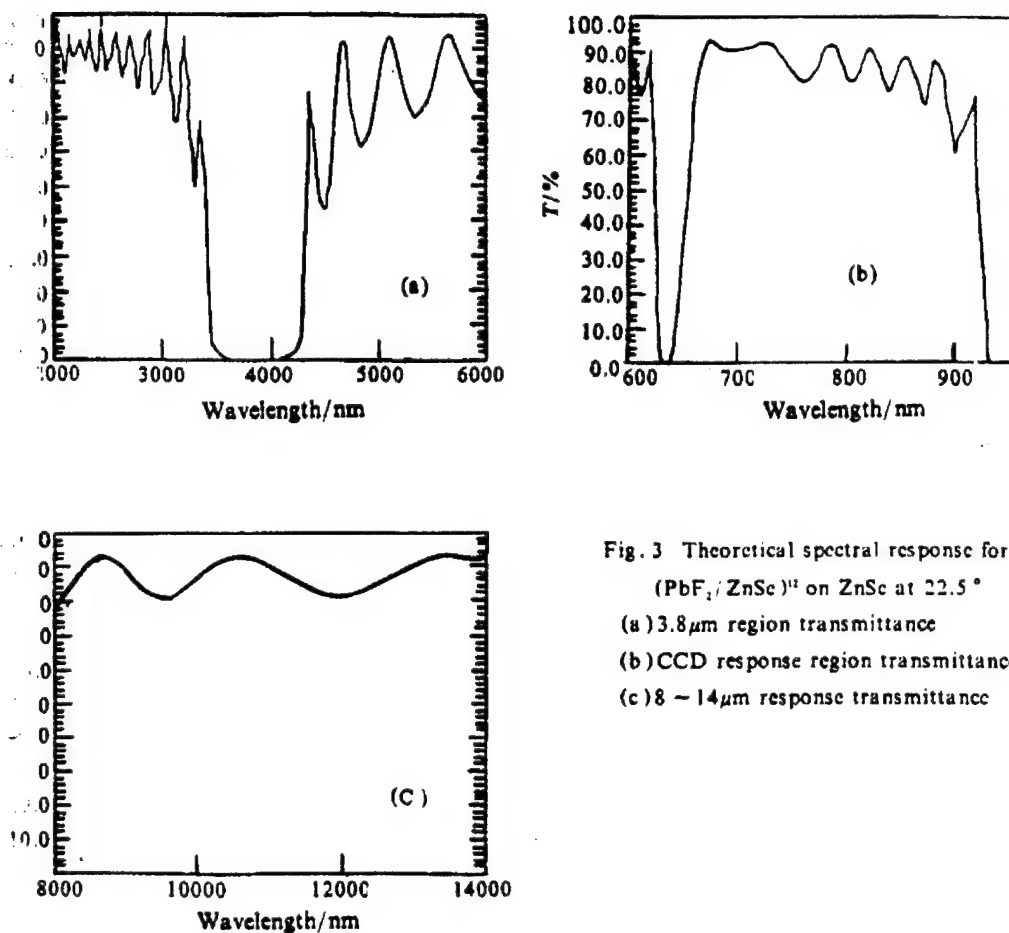reduced-reflectance film with two widely separated wavebands

38

Fig. 3 Theoretical spectral response for
(PbF₂/ZnSe)¹² on ZnSe at 22.5°
(a) 3.8μm region transmittance
(b) CCD response region transmittance
(c) 8 ~ 14μm response transmittance

between the visible light region and the infrared region between 8 and 14μm, in order to eliminate the reflectivity wear onback. Table 2 shows a trichroic spectroscopic film Sub/(4L6H)¹²/Air in a single-surface ZnSe substrate; at the back, there are the expected properties of the reduced-reflectance film. As shown in Table 2, the required properties can be satisfied by combining these two kinds of films.

39

Table 2 Theoretical coating designs for 22.5° incident on ZnSe
for a 3.8μm reflecting trichroic beam splitter

DF laser response				
fiector ating esign	optical thickness at $3.8\mu m$	reflectance (%)	$3.6 \sim 4.2\mu m$ average transmittance (%)	absorptanc (%)
F$_2$/ ZnSe)^2	(0.20/0.30)	99.92	0.03	0.05
long wavelength band and visible CCD response				
AR coating design	optical thickness at $0.76\mu m$	$8 \sim 14\mu m$ average transmittance* (%) goal predicted		$0.64 \sim 0.92\mu m$ ave transmittance* (goal predicte
S/ PbF$_2$/ BaF$_2$)	(0 25/3.0/0.25)	80 88		80 88

* Total includes both surfaces

IV. Experiments

To prepare a high-quality, low-absorptance surface, carving
and polishing were used to grind and polish the OD50mm CVD ZnSe
so that a good (0.1 diaphragm) and 0.5′ parallelism can be
obtained at the substrate surface. The post-polishing substrate
was washed with a mixture of ethyl alcohol and ethyl ether; after
drying with nitrogen, the substrate was immediately placed into a
film-coating chamber. Prior to film coating, an Ar$^+$ ion beam was
used to bombard the substrate for 20min to further remove dirt
from the surface. The ion beam energy was 300ev and the beam
current density was 20mA/cm^2.

The thin-film deposition was done in an AQ700 film-coating
machine; gases were evacuated from the machine with a
turbomolecular pump so that the vacuum was free of contamination.

A spherical-surface rotating jig was used to improve film layer homogeneity. The degree of vacuum with the instrument was 10^{-3}Pa. There was a hot-cathode ion source installed in the film-coating machine for ion-beam supplementary deposition. Both PbF_2 and ZnSe were deposited with the electron beam. The PF_2 deposition gas pressure was 6.2×10^{-3}Pa and the ZnSe gas deposition pressure was 3.4×10^{-3}Pa. The substrate temperature was 160°C. The film thickness was controlled with an optoelectronic limit value method, with a control wavelength of 0.76μm. A quarter-layer of ZnSe film at 0.76μm was coated in advance on a K9 glass control plate; the method of multiple limiting values was used to control the spectroscopic film.

V. Results of Experiments

On the front surface of the ZnSe substrate, a trichroic spectroscopic film of reflection at 3.8μm (as mentioned in Table 2) was deposited. By using a Perkin-Elmer 350 infrared spectrophotometer, the infrared transmission spectrum of the coated specimen was measured. By measuring the central position of the reflection band, the film layer thickness was examined. By adjusting the control wavelength, the center of the reflection band was placed at 3.8μm. Since the reflection band width is difficult to measure the position of maximum reflectance in the reflection band, the authors measured two wavelengths when the transmittance rose to 1%. The mean value of these two wavelengths was defined as the center wavelength.
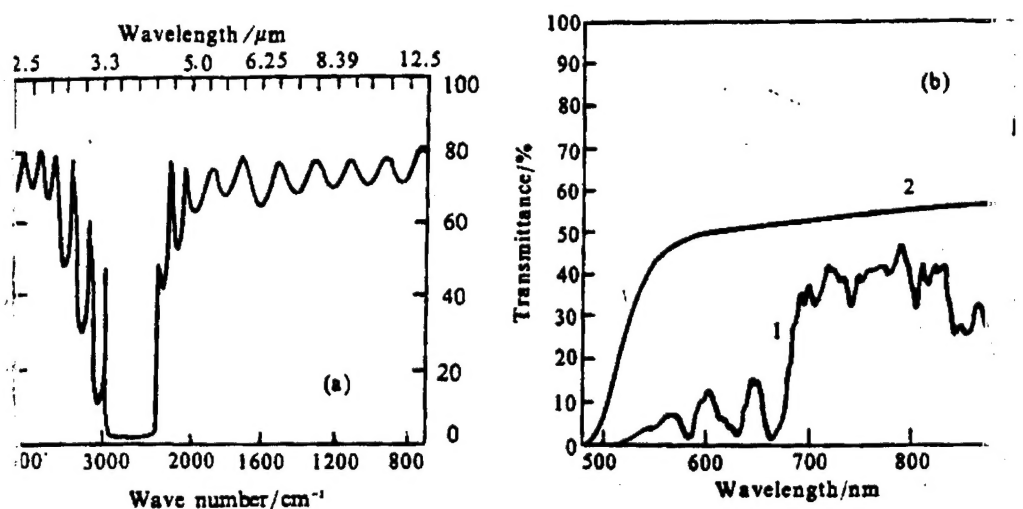
41

Fig. 4 Measured spectral performance of ZnSe 3.8μm reflecting trichroic beam splitter

a. 3.8μm band and 8 ~ 14μm long wavelength performance

b. (1)0.5 ~ 0.9μm visible spectral performance ; (2)transmittance of uncoated ZnSe substra

Film thickness is controlled with multiple limiting values by using transmitted light. The controlled wavelength was determined by a grating monochromator. After multiple experiments, consideration was given to chromatic dispersion of the film-coating material, as well as the difference in the deposition thickness between the control substrate and the specimen; finally, the film thickness was controlled at 0.76μm wavelength. Fig. 4 indicates the spectral experimental properties of the coated specimens in the infrared zone and the visible light zone. As shown in the figure, under the condition that the reduced-reflectance film is not coated on the back of the ZnSe substrate, and the high-reflectance band is in the range

42

between 3.4 and 4.2μm wavelength, with mean transmittance less than 0.4%, the measured reflectance at 3.8μm is greater than 99.6%; and the mean transmittance in the spectral region between 8 and 14μm is greater than 75%; and the mean transmittance in the visible-light spectral region between 0.64 and 0.92μm is close to 50%. If a reduced-reflectance film with the widely separated dual wavebands is coated on the back of ZnSe as mentioned in Table 2, the transmittance properties in the visible-light spectra and the spectral region between 6 and 14μm will be further improved.

While making the optical property measurements on the film layers, the authors evaluated the environmental stability and the adherence property of the film layers. The stability experiments were conducted as per International Standard GB 1317-77. The film layer experiments involved moisture in the air, low temperature, and saline water. After these experiments, the optical properties of the film layers remained unchanged. With adherence force examination of the film layers by using adhesive tape, the adhesive tape was unable to separate the film layers.

The authors conducted two coating methods on the film deposition. One involved general thermal evaporation. In the other method, while thermal evaporation took place, Ar^+ ion-beam bombardment was conducted; the bombardment beam current was 60mA. It was discovered that under a spotlight with high transmission in the visible-light region and high thermal evaporation in the trichroic spectroscopic film with ion-beam supplementary

43

deposition, the optical scattering was obviously less than that
for the thermally-evaporated film. This is possibly explained by
the fact that the bombardment film was denser than the evaporated
film, and the coarseness was less than that of the evaporated
film.

The first draft of the article was received on June 1, 1993;
the final revised draft was received for publication on July 30,
1993.

REFERENCES

Rudisill JE, Bernardo Garcia, Bradley Bobbs L, and Morris Braustein. *Appl Opt*,
980, 19 (13): 2121 ~2127.

Dodge MJ. Laser Induced Damage in Optical Materials, 509, NBS Special Publica
1977, 83 ~88.

Solomon Musikant. *Optical Materials*. (Marcel Dekker, Inc, 1985), 112.

Harrington JA, Rudisill JE, and Braustein M. *Appl Opt*, 1978, 17 (17): 2798 ~2800.

Macleod HA. *Thin Film Optical Filters*. (Second edition). Adm Hilget Ltd, Bristol,

DISTRIBUTION LIST

DISTRIBUTION DIRECT TO RECIPIENT

ORGANIZATION	MICROFICHE
BO85 DIA/RTS-2FI	1
C509 BALL0C509 BALLISTIC RES LAB	1
C510 R&T LABS/AVEADCOM	1
C513 ARRADCOM	1
C535 AVRADCOM/TSARCOM	1
C539 TRASANA	1
Q592 FSTC	4
Q619 MSIC REDSTONE	1
Q008 NTIC	1
Q043 AFMIC-IS	1
E404 AEDC/DOF	1
E410 AFDTC/IN	1
E429 SD/IND	1
P005 DOE/ISA/DDI	1
1051 AFIT/LDE	1
PO90 NSA/CDB	1

Microfiche Nbr: FTD96C000216
NAIC-ID(RS)T-0508-95